IOP Publishing — Nanotechnology
Nanotechnology **18** (2007) 465304 (8pp) doi:10.1088/0957-4484/18/46/465304

Controlling thin film structure for the dewetting of catalyst nanoparticle arrays for subsequent carbon nanofiber growth

S J Randolph[1,2], J D Fowlkes[1,2], A V Melechko[2], K L Klein[1,2], H M Meyer III[2], M L Simpson[1,2] and P D Rack[1,2,3]

[1] University of Tennessee, 434 Dougherty Hall, Knoxville, TN 37996, USA
[2] Oak Ridge National Laboratory, PO Box 2008, Oak Ridge, TN 37831, USA

E-mail: prack@utk.edu

Received 23 August 2007, in final form 20 September 2007
Published 17 October 2007
Online at stacks.iop.org/Nano/18/465304

Abstract
Vertically aligned carbon nanofiber (CNF) growth is a catalytic chemical vapor deposition process in which structure and functionality is controlled by the plasma conditions and the properties of the catalyst nanoparticles that template the fiber growth. We have found that the resultant catalyst nanoparticle network that forms by the dewetting of a continuous catalyst thin film is dependent on the initial properties of the thin film. Here we report the ability to tailor the crystallographic texture and composition of the nickel catalyst film and subsequently the nanoparticle template by varying the rf magnetron sputter deposition conditions. After sputtering the Ni catalyst thin films, the films are heated and exposed to an ammonia dc plasma, to chemically reduce the native oxide on the films and induce dewetting of the film to form nanoparticles. Subsequent nanoparticle treatment in an acetylene plasma at high substrate temperature results in CNF growth. Evidence is presented that the texture and composition of the nickel thin film has a significant impact on the structure and composition of the formed nanoparticle, as well as the resultant CNF morphology. Nickel films with a preferred (111) or (100) texture were produced and conditions favoring interfacial silicidation reactions were identified and investigated. Both compositional and structural analysis of the films and nanoparticles indicate that the properties of the as-deposited Ni catalyst film influences the subsequent nanoparticle formation and ultimately the catalytic growth of the carbon nanofibers.

(Some figures in this article are in colour only in the electronic version)

1. Introduction

Processing methods that enable the assembly of carbon nanotubes (CNTs) and nanofibers (CNFs) into functional nanoscale structures are critical for nanoscale science and technology [1–4]. Furthermore, the ability to encapsulate various materials within these nanostructures provides a unique opportunity to control the physical properties of nanoscale materials in a variety of environments and phases [5–9]. One method that offers a wide degree of freedom in controlling carbon nanostructure synthesis is catalytic chemical vapor deposition [10]. In this method, catalyst nanoparticles are prepared on the substrates and the synthesis proceeds through catalytic decomposition of carbonaceous gas into graphitic carbon structure. Fortuitously, most of the catalytic metals used in carbon nanostructure synthesis are well known ferromagnets, which makes such co-synthesis attractive for such applications as magnetic information storage or nanoscale transducers for biomedical applications [11–14]. The catalyst

[3] Author to whom any correspondence should be addressed.

 © 2007 IOP Publishing Ltd Printed in the UK

particles can be prepared by the dewetting of a continuous thin film. Using photo- or electron-beam-lithography the nanoparticles can be defined at specific locations on the substrate [10].

Dewetting is the process in which a continuous wetting or non-wetting thin film is treated under conditions that allow the system to minimize its interfacial energy by breaking up into separate particles or 'islands'. Typically, energy must be applied to the metastable film/substrate systems in order to facilitate the dewetting process. Dewetting of thin polymer films has been observed by heating above the glass transition temperature [15], and metallic thin films have been dewetted by ion bombardment [16, 17], pulsed laser [18, 19], and oxygen plasma treatment [20]. The thickness of the film and its wetting properties dictate the mechanism by which dewetting occurs; nucleation of holes in the film or spinodal dewetting [21] are possibilities for non-wetting films, whereas wetting films can proceed by nucleation and growth of smaller particles [18, 22]. Redon *et al* have provided a thorough theoretical and experimental analysis using oil films on silicon as a model for studying the dewetting mechanism and dynamics [23].

The film/substrate choice as well as the catalyst film thickness may be used as controls for directing the size of the resultant nanoparticles. This is a critical means to control CNT and/or CNF synthesis, and when used in conjunction with lithographic patterning both the location and the number of nanostructures at each site may be pre-determined.

While this type of control is very useful, there still exists an unexplored dimension of nanoparticle and carbon nanostructure synthesis. The role that the thin film deposition parameters and the initial thin film properties have on the resultant nanoparticle/nanostructure has gone largely unstudied. For instance, it is possible to control the crystallographic orientation and/or composition of catalyst nanoparticles by controlling the texture of the original thin film. Indeed, recent studies by Fowlkes *et al* have shown that the initial (111) orientation of sputter-deposited nickel catalyst films may be preserved throughout the dewetting process to the CNF growth process, where faceting of nickel nanoparticle-terminated CNFs was observed corresponding to the initial texture orientation of the sputtered thin film [24]. The observation that texturing may be preserved through a high temperature, plasma-enhanced chemical vapor deposition (PECVD) process is not necessarily intuitive and warrants further investigation.

Here, we have investigated several rf magnetron sputter deposition process conditions in order to control the texture and silicidation of nickel thin films on single-crystal (111)-Si. The initial film properties have been correlated to the dewetting/nanoparticle formation process and ultimately to changes in the CNF morphology.

2. Experimental details

In this work, all nickel thin films were deposited on (111)-oriented, single-crystal, 100 mm, silicon wafers. Films were deposited on the polished silicon surface and no pretreatment of the silicon wafers was performed to remove the native silicon oxide prior to deposition.

Nickel thin films were deposited using a 5 cm diameter rf sputtering source with a magnetic mode magnetron configuration for depositing magnetic materials. Nickel foils of 99.994% purity and 0.5 mm thickness (Alfa-Aesar) were used as the target material, and were bonded to a copper backing plate.

Common sputter deposition conditions that were used include 200 W rf plasma power with a gas flow rate of 25 sccm of Ar/H_2 at a ratio of 95/5%. An average target-to-substrate distance was maintained at $\sim$13 cm and substrate rotation was employed to enhance the film uniformity (see Fowlkes *et al* [25, 26] for a complete system description). Nickel deposition rates were determined to be $\sim$4.4 nm min^{-1}, and the deposition time was chosen to yield 25 nm thick films in all cases. Variable sputter parameters included substrate temperature, substrate bias, and sputter gas pressure.

Dewetting of the catalytic nickel films as well as CNF growth were performed in a 100 mm diameter dc plasma-assisted CNF growth chamber. Each catalyst-coated wafer was cleaved to a $\sim$2 cm $\times$ 2 cm size so all the various catalyst sputtering conditions could be processed in a single dewetting/VACNF growth cycle to minimize experimental variations. For the dewetting process, the pieces were heated to 700 °C in ammonia atmosphere at 5 Torr, prior to initiation of the NH_3 plasma. Subsequently the catalysts were exposed to an NH_3 plasma under the following conditions: 80 sccm NH_3, a current of 400 mA (constant current mode $\sim$ 500 V), and a process time of 1 min. Subsequent to evaluating the properties of the dewetted Ni catalyst, a VACNF growth was performed under the following growth conditions: acetylene flow rate of 35 sccm, NH_3 flow rate of 80 sccm, total pressure of 5 Torr, 400 mA of DC current, and a growth time of 20 min then later an additional 45 min growth under the same conditions.

Structural characterization of the samples was performed on a Panalytical X'Pert diffractometer using Cu Kα x-rays in the standard $\theta/2\theta$ configuration. The diffractometer x-ray source was operated in line mode and 1° divergence and receiving slits were employed for all scans. Panalytical's HighScore software package was utilized for x-ray diffraction (XRD) peak identification and smoothing. An external MATLAB program was written to apply thin film corrections to each scan, which correct for the variation in the probed volume of the thin film as a function of the incident x-ray beam angle. All scans ranged from $2\theta = 43°$ to 80°.

Electron microscopy and microanalysis was performed in order to obtain both compositional and morphological information. A scanning Auger microprobe (SAM, PHI 680) was used to analyze near surface atomic concentrations, as well as for compositional depth profiling. A Hitachi S-4700 field emission scanning electron microscope (SEM) was used for imaging and morphological characterization.

3. Results and discussion

During sputter deposition, energetic ions and neutrals impart momentum to the target material, which eject near surface atoms that condense on a close proximity substrate. The energetic nature of sputtering typically imparts a high degree of residual stress to the deposited films. Such is the case for nickel thin films, where the sputtered film may remain in a

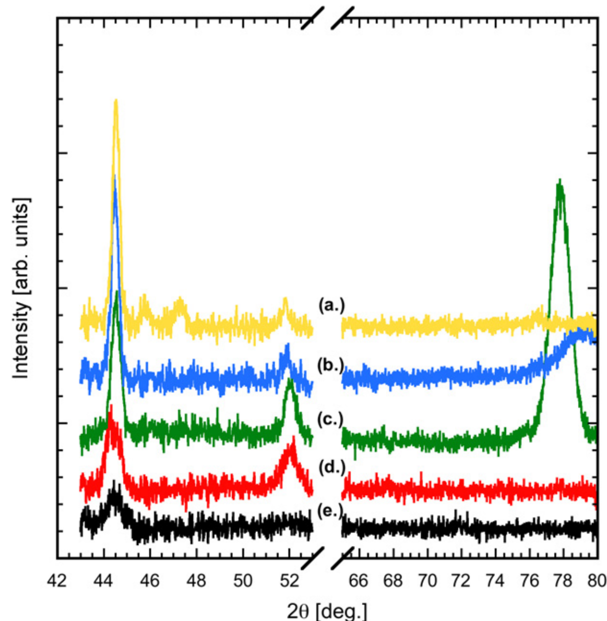

Figure 1. XRD scans of as-deposited sputtered nickel films.

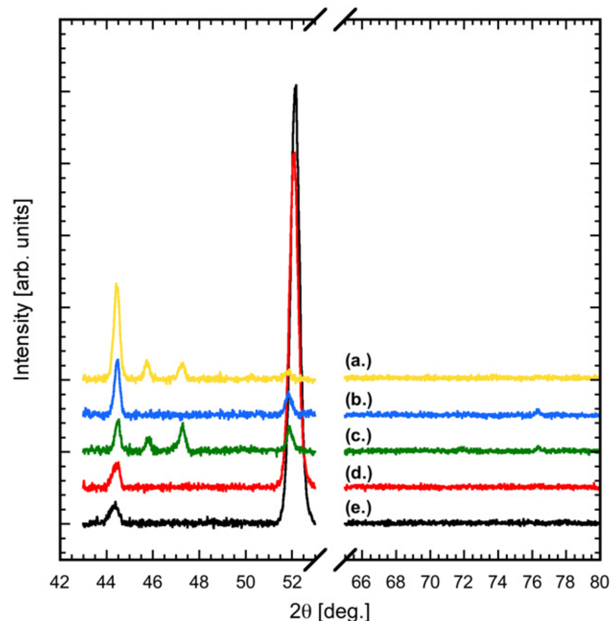

Figure 2. XRD scans of nickel nanoparticles formed by dewetting nickel films.

metastable state due to the strain energy associated with the film–substrate confinement and intrinsic film stresses. In many cases, strain energy relaxation can be manifest in preferred crystallite orientation, where a certain strain energy magnitude favors the transition of the film to a preferred orientation [24]. Both pressure and substrate bias affect the energetic atom/ion bombardment, and as a result change the residual stress in nickel thin films [27].

Three common parameters that may be used to modify sputtered thin film properties are substrate temperature, substrate bias, and sputter gas pressure. These variables, in addition to affecting film stress, may also alter the film composition and phase formation due to the reactivity and/or intermiscibility of the deposited nickel and silicon from the substrate. Interfacial nickel silicidation reactions are energetically favorable and quite common, as evidenced by a large body of literature focusing on the formation kinetics and characterization [28, 29] of a variety of nickel silicide phases. The plethora of possible silicide phases complicates understanding the effects of the initial film state on the resultant nanoparticle.

In order to evaluate the effects of the initial nickel thin film properties on the subsequent, dewetted nanoparticle and CNF properties, it was necessary to thoroughly investigate the film deposition parameters. The development of the specific process conditions as described in this work involved an initial statistical design of experiments (DoE). The DoE was created in the JMP© statistical package (see http://www.jmp.com/ for information) using the built-in customizer, where a three-level DoE was chosen to allow for quadratic effects. The factors chosen were the pressure (3, 6.5, 10 mTorr), substrate bias (0, −50, −100 V), and temperature (28, 214, 400 °C). The responses chosen were the (200) nickel integrated intensity and the ratio of the nickel (200) to the nickel (111) integrated intensities. Upon XRD analysis of the DoE results, silicidation of the films deposited at more energetic conditions presented

Table 1. Varied nickel sputter deposition parameters.

ID	Pressure (mTorr)	Substrate bias (V)	Substrate temperature (°C)
a	3	−100	400
b	6.5	−50	400
c	3	0	300
d	10	0	214
e	10	0	28

difficulties in quantification of preferred orientation due to the appearance of this additional variable. Therefore, the results of the DoE were confined to the lower energy conditions where silicidation did not take place. From this data, conditions likely to favor both (111) and (100) nickel orientations were extracted. In addition, qualitative analysis of the x-ray and SEM data was used to determine conditions that yielded silicide formation. From this design of experiments, five unique parameter sets were chosen to illustrate the effects that the initial film crystallinity, composition, and orientation has on the subsequently formed nanostructures. The variable parameters used to deposit these five 25 nm thick Ni samples are listed in table 1.

XRD analysis of the as-deposited films was performed following the deposition of the films. These XRD scans are shown in figure 1. The broken axis in figure 1 is intentional so as to not show the strong (222) reflection from the underlying (111)-oriented silicon substrate. For all samples, it is evident from the low signal-to-noise ratio that the overall crystallinity is relatively low and is further exacerbated by the 25 nm thickness. As expected, increasing the temperature of the deposition process appears to increase the overall crystallinity, as demonstrated by the increase in the diffracted signal levels.

Comparing figures 1(a)–(c) it is clear that the film texture has changed. The progression from condition (a) to (b), is associated with a change in ion bombardment during film

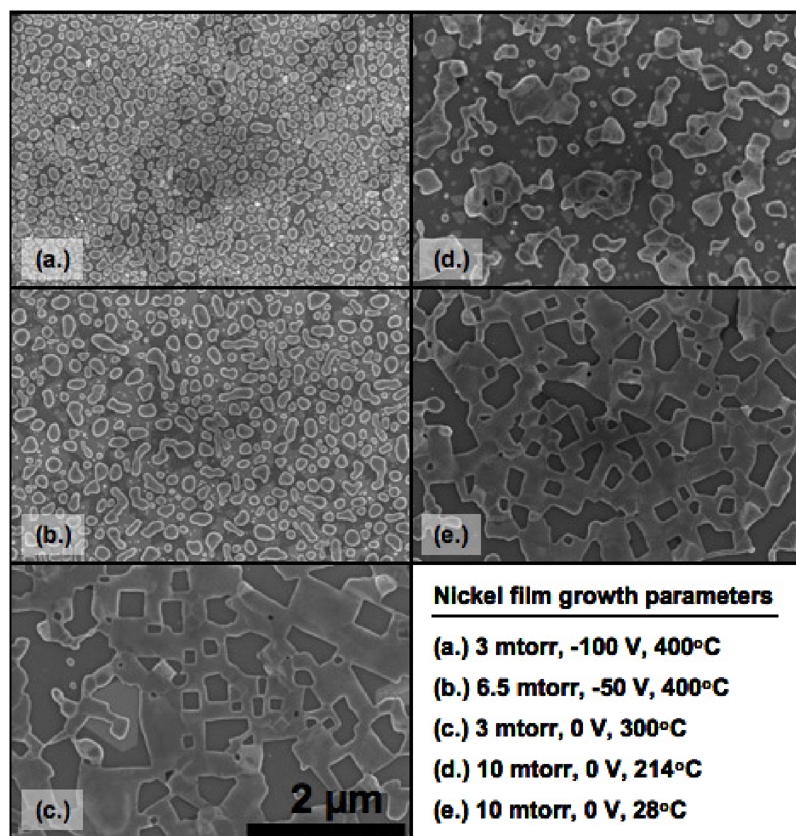

Figure 3. Top-view SEM images of nickel nanoparticles formed by dewetting nickel films.

growth (constant growth temperature). Specifically, lower pressure and higher substrate bias favors ion bombardment from the higher energy distribution of sputtered species and induced bias, respectively. Progression to condition (c) has a slightly lower temperature and likely lower ion bombardment because no substrate bias was applied. While figures 1(d) and (e) only reveal the nickel (111) and (200) at ∼44.5° and ∼52.2°, respectively, additional peaks are clearly observed in figures 1(a)–(c). Due to the high noise levels and the existence of several nickel silicide phases, these XRD peaks were not indexed definitively. However, based upon the peak search routines in the Panalytical HighScore software, these first three films are most likely a combination of FCC Ni, Ni_2Si, and $Ni_{1.5}Si$. Based solely on the temperatures of these first three films, this is consistent with the order of formation of nickel silicides [28, 29], which typically proceeds from Ni_2Si to NiSi to phases of higher silicon content with increasing temperature.

The XRD patterns of the final two films (figures 1(d) and (e)) were grown using much lower energetic conditions (lower energy, no substrate bias, and higher pressure, which lowers the energy distribution of sputtered species), and are observed to be only nickel. However, an increase in substrate temperature from room temperature to 214 °C drives the preferred orientation from (111) to (100), as determined by the ratio of integrated intensities of their (111) and (200) peaks. It is noted that the (100) reflection is prohibited in an FCC system. It is presumed that the elevated substrate temperature in figure 1(d) induces a residual stress due to differential thermal expansion that is not present in figure 1(e). The coefficient of linear thermal expansion (CTE) of silicon is $\sim 3\times10^{-6}$ K^{-1} and that of nickel is $\sim13\times10^{-6}$ K^{-1}. Since the strain at room temperature can be approximated as the product of the differences of the CTE and the difference in deposition temperature to room temperature, the thermally induced strain in this film is estimated to be $\sim1.86\times10^{-3}$. Similar to previous works, it is thought that the induced strain energy is relaxed through reorientation of the nickel crystallites [24].

Following the XRD analysis of the as-deposited films, the wafers were cleaved into smaller pieces, and the plasma dewetting process was carried out. After dewetting into nickel nanoparticles, the samples were characterized in the scanning electron microscope (SEM) and using XRD.

The XRD scans of all five nanoparticle samples are shown in figure 2. Intuitively, the crystallinity of all samples increased dramatically after the high temperature dewetting process, as evidenced by the higher signal-to-noise ratio. The scans in figures 2(a) and (c) show a pattern that is again characteristic of a high nickel content silicide. Notably, these two initial films were the only samples prepared at 3 mTorr. As operating at lower pressure reduces the amount of gas-phase scattering, the condensing species tend to have a higher kinetic energy when reaching the substrate. According to this result, lower pressures would appear to be a critical factor in determining whether or not silicidation occurs in this 300–400 °C temperature range. For instance, the sample referenced by figure 2(b) has very similar conditions to figure 2(a), but the most significant variable change is the higher operating pressure. The result of this scan indicates that

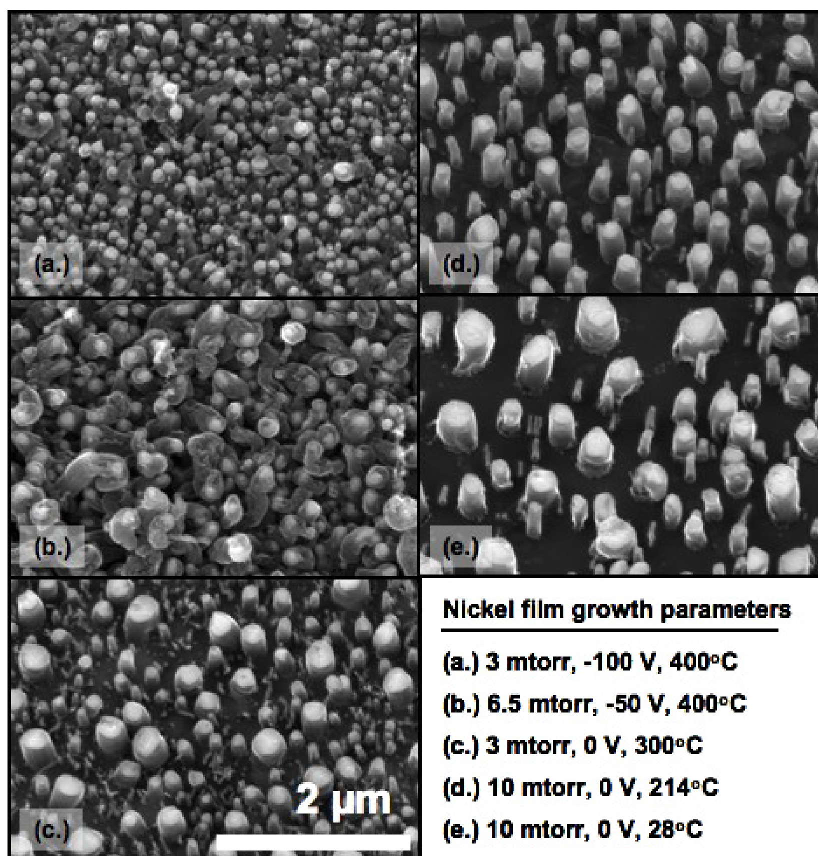

Figure 4. 20° tilted SEM images of the final stage of nanoparticle formation after a 20 min VACNF growth. Nanoparticles are visible as brighter regions on top of short carbon stumps.

the film is nearly randomly oriented nickel, with no discernible silicide peaks. This scan along with figure 2(c) are the only two samples with a detectable nickel (220) peak located at ~76.4°.

Perhaps the most startling effects observed in figure 2 are in regards to the final two samples. Both figures 2(d) and (e) show an extraordinarily high degree of preferred nickel (100) orientation (as evidenced by the high (200) integrated intensity). Based on the as-deposited state of the film, it would appear that all of the initially amorphous nickel must have rearranged to crystalline, (100)-oriented nickel. The lower overall crystallinity observed in figures 2(a)–(c) is consistent with the fact that the silicides have higher melting temperatures and thus inhibit crystallization of both Ni and $NiSi_x$ phases during the dewetting procedure.

In addition to the structural differences, the electron micrographs in figure 3 illustrate the dramatic differences in the morphology of the dewetted nanoparticles. The morphologies of the samples shown in figures 3(a) and (b) are very similar, with particles having smooth, rounded edges and the substrate consisting of light and dark regions as viewed in the SEM. It was suspected that the surface color variations were due to separation of silicide phases, and to verify this Auger microanalysis was employed. While the results were inconclusive as to the specific stoichiometries that were present, it was verified that in all cases the nanoparticles were indeed much higher in nickel content than the substrate surface. This observation is particularly useful when placed in the context of recent work [30] regarding the effects of silicidation on nanoparticle carbon catalytic behavior. Esconjauregui *et al* elucidated the effects of silicidation on CNT growth and determined that utilizing certain pretreatment and growth parameters resulted in highly active metal silicide, as well as pure metal, nanoparticles [30].

Another noteworthy observation regarding these two samples is that the more energetic deposition process (figure 3(a)) leads to smaller particles with a higher surface population density. Recently, in an investigation of germanium nanocrystal formation, it was noted that stress-induced dewetting resulted in lower temperature dewetting than a thermally activated process alone [31]. The germanium–silicon lattice mismatch strain was used to induce strain energy on a thin silicon-on-insulator (SOI) structure. This induced stress lowered the temperature threshold for dewetting of the silicon film in the SOI structure. It is thought that an analogous stress-enhanced mechanism may be responsible for the change in dewetting properties of the films observed here.

The most striking morphological result is shown in figure 3(c), where faceting of the dewetted films appears to occur with a preferred shape and direction. Clearly, rectangular holes in the film are visible, many of which are aligned along common axes in the plane of the surface. This type of formation was unique to this sample and was found in isolated regions of the film. To our knowledge, this type of structure has not been reported in the metallic dewetting literature. Similar

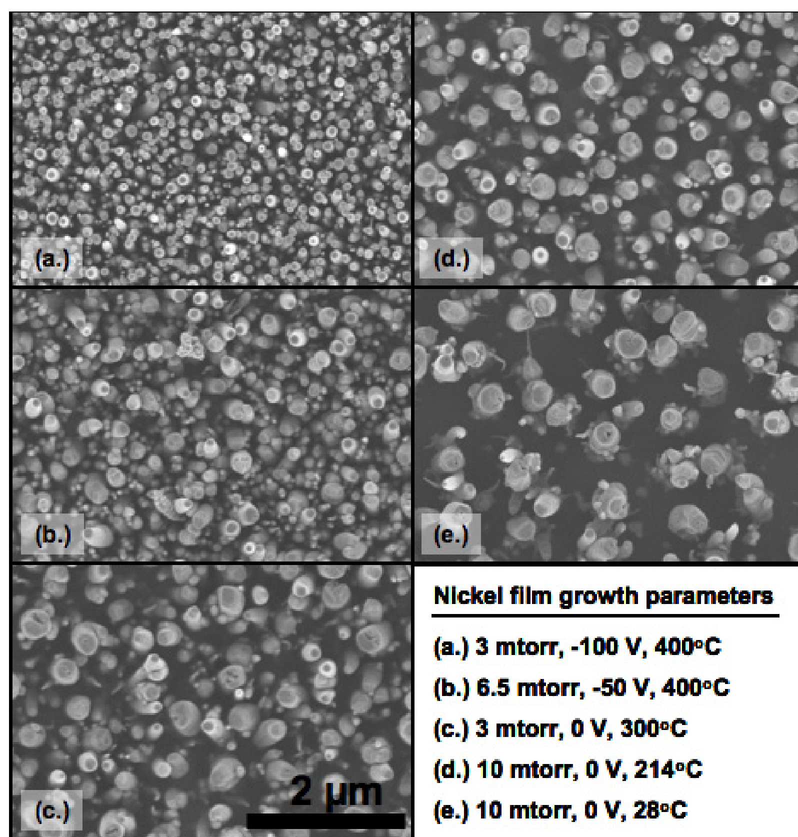

Figure 5. Top-view SEM images of carbon nanofibers following the 45 min growth.

morphology is observed in figure 3(e), yet there seems to be a notable absence of the in-plane alignment. Since the deposition conditions influence the occurrence of these aligned structures as in figure 3(c), it stands to reason that conditions may exist that would lead to this being a preferred feature, as opposed to selective regions on the sample.

Whereas the dewetted films shown in figures 3(c) and (e) are similar in that the particle/film surface appears to be smooth and faceting occurs in the 'holes', faceting is apparent in the 'particles' shown in figure 3(d). Here, the particles are rough and appear to be highly crystalline and faceted. The substrate surface of the sample in figure 3(d) is also covered with 'highlighted' regions of higher secondary electron brightness, which were assumed to be embedded, epitaxial nickel silicide formed during the dewetting process. Again, Auger analysis was quantitatively inconclusive; however, it showed that the bright regions were nickel-rich silicides compared to the darker substrate regions, which were mainly silicon.

Following the dewetting process, the next phase of nanoparticle formation involves interaction with graphitic carbon. The initial stage has been shown to involve the formation of flat graphitic layers between the nanoparticles and the substrate, bending of graphene layers at the edges and reshaping of nanoparticles [32, 33]. To demonstrate the final stage of nanoparticle formation and the initial stages of fiber growth we performed a relatively short growth (20 min) of nanofibers presented in figure 4. Finally, an additional 45 min long CNF growth was performed on all five samples and the results were analyzed via SEM. These results are shown in figure 5 (normal to surface) and figure 6 (tilted at 30°). The most prominent effects appear to have been on the nanofiber diameter, height, and spatial distributions. The average height (and standard deviation) of the fibers after the second 45 min growth were determined to be (a) 1.95 μm (0.33 μm), (b) 1.81 μm (0.31 μm), (c) 1.81 μm (0.12 μm), (d) 2.32 μm (0.32 μm), and (e) 2.16 μm (0.18 μm). The average size of nanoparticles (and hence nanofiber diameters) is varied in a wide range for the same initial film thickness. This result means that the previously reported dependences of the average size on film thickness are specific only to the particular deposition conditions used in these reports and are not universal [34, 35]. Also one of the very important implications is that if the film is patterned into arrays of disks, the number of particles per site will depend not only on the diameter of the disks and the film thickness but also on the film deposition conditions [10]. This observation is very important for synthesis of the arrays of single freestanding VACNFs in such applications as focused electron field emission sources [36]. While the 'high deposition energy' samples shown in figures 4(a) and (b) have a higher number of fibers per unit area and a smaller average diameter (consistent with the dewetting and initial growth images), the height distribution appears to be broader. Specifically, there are sporadic individual fibers which clearly are taller than the rest. In contrast, in conditions in which lower energy is applied to the substrate, the films yielded CNFs with larger diameters, but more uniform in height, as in figures 4(c) and (e). This fact corresponds to the possible link between

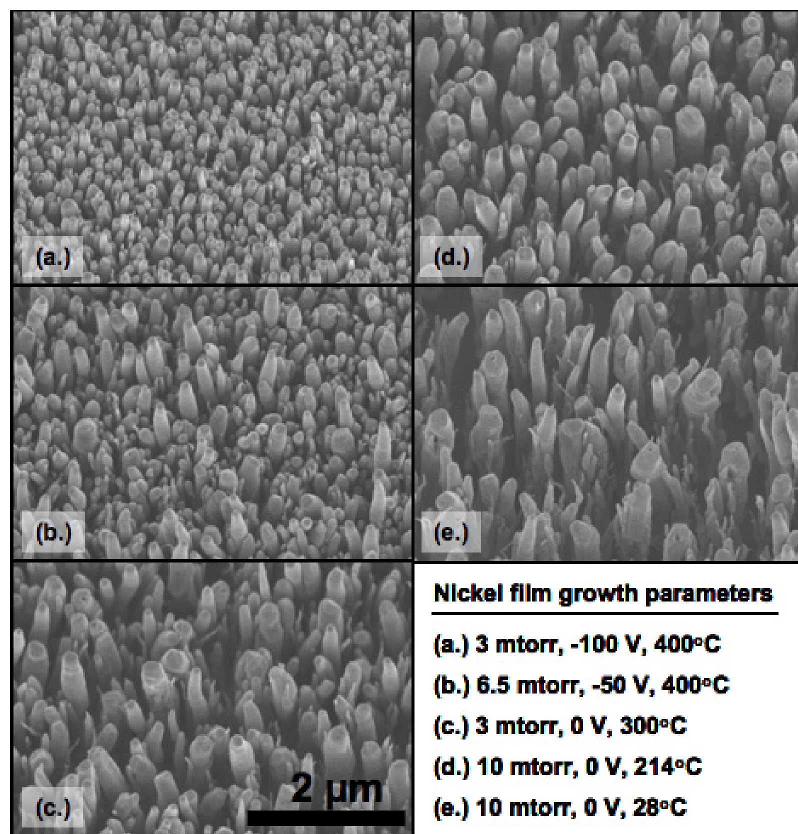

Figure 6. 30° tilted SEM images of carbon nanofibers following the 45 min growth.

the nanoparticle crystallographic orientation and the nanofiber growth rate. Other evidence of this correlation is being published elsewhere [37], but it is important to note that this present work is consistent with this. Practically, the ability to control the orientational texture of the films and consequently the nanoparticles translates into the possibility of controlling the height distribution of the VACNF arrays. This ability is highly desirable for many applications that are sensitive to the height variations between elements of the array. As such, these results indicate that controlling the initial catalyst film properties is another dimension to control the catalytic co-synthesis of nanoparticles and nanofiber systems.

4. Conclusions

We have presented evidence for the ability to influence nickel nanoparticle and carbon nanofiber properties by modification of the as-deposited nickel thin film. A set of rf magnetron sputter deposition parameters are used to produce (111)-textured, (100)-textured, as well as nickel silicide thin films as seed layers for nanoparticle formation.

We have also shown that the level of energy used to deposit the nickel films not only influences the crystallite orientation and level of silicidation of the catalyst film, but also the resultant crystal structure, shape, aereal density and size distribution of nanoparticles formed by plasma-assisted dewetting of the nickel-on-silicon system. This effect is reflected in the geometry of nanofiber arrays and the nanofiber morphology. The mechanisms underling this relationship are the subject of future investigations.

Acknowledgments

The authors acknowledge the support of the Microsystems Technology Office of DARPA. AVM and MLS acknowledge support from the Material Sciences and Engineering Division Program of the DOE Office of Science. A portion of this research was conducted at the Center for Nanophase Materials Sciences, which is sponsored at Oak Ridge National Laboratory by the Division of Scientific User Facilities, US Department of Energy.

References

[1] Ajayan P M and Zhou O Z 2001 *Carbon Nanotubes* **80** 391–425
[2] Melechko A V, Merkulov V I, McKnight T E, Guillorn M A, Klein K L, Lowndes D H and Simpson M L 2005 *J. Appl. Phys.* **97** 41301–1
[3] Terrones M 2003 *Ann. Rev. Mater. Res.* **33** 419–501
[4] Terrones M and Terrones H 2003 *Phil. Trans. R. Soc.* A **361** 2789–806
[5] Golberg D, Gu C Z, Bando Y, Mitome M and Tang C C 2005 *Acta Mater.* **53** 1583–93
[6] Golberg D, Mitome M, Muller C, Tang C, Leonhardt A and Bando Y 2006 *Acta Mater.* **54** 2567–76
[7] Muller C, Golberg D, Leonhardt A, Hampel S and Buechner B 2006 *Phys. Status Solidi* a **203** 1064–8
[8] Muller C, Hampel S, Elefant D, Biedermann K, Leonhardt A, Ritschel M and Buchner B 2006 *Carbon* **44** 1746–53

[9] Elias A L *et al* 2005 *Nano Lett.* **5** 467–72
[10] Merkulov V I, Lowndes D H, Wei Y Y, Eres G and Voelkl E 2000 *Appl. Phys. Lett.* **76** 3555–7
[11] Thompson D A and Best J S 2000 *IBM J. Res. Dev.* **44** 311–22
[12] Mornet S, Vasseur S, Grasset F and Duguet E 2004 *J. Mater. Chem.* **14** 2161–75
[13] Bauer L A, Birenbaum N S and Meyer G J 2004 *J. Mater. Chem.* **14** 517–26
[14] Hamad-Schifferli K 2004 *Biophys. J.* **86** 481a
[15] Reiter G 1992 *Phys. Rev. Lett.* **68** 75–8
[16] Bolse T, Elsanousi A, Paulus H and Bolse W 2006 *Nucl. Instrum. Methods Phys. Res.* B **244** 115–9
[17] Hu X Y, Cahill D G and Averback R S 2000 *Appl. Phys. Lett.* **76** 3215–7
[18] Bischof J, Scherer D, Herminghaus S and Leiderer P 1996 *Phys. Rev. Lett.* **77** 1536–9
[19] Favazza C, Kalyanaraman R and Sureshkumar R 2006 *Nanotechnology* **17** 4229–34
[20] Han G C, Wu Y H, Luo P, Qiu J J and Chong T C 2003 *Solid State Commun.* **126** 479–84
[21] Herminghaus S, Jacobs K, Mecke K, Bischof J, Fery A, Ibn-Elhaj M and Schlagowski S 1998 *Science* **282** 916–9
[22] Brochard-Wyart F and Daillant J 1990 *Can. J. Phys.* **68** 1084–8
[23] Redon C, Brochard-Wyart F and Rondelez F 1991 *Phys. Rev. Lett.* **66** 715–8
[24] Fowlkes J D, Melechko A V, Klein K L, Rack P D, Smith D A, Hensley D K, Doktycz M J and Simpson M L 2006 *Carbon* **44** 1503–10
[25] Fowlkes J D, Fitz-Gerald J M and Rack P D 2006 *Thin Solid Films* **510** 68–76
[26] Fowlkes J D, Fitz-Gerald J M and Rack P D 2007 *Thin Solid Films* **515** 3488–98
[27] Alfonso J A, Greaves E D, Lavelle B and Sajo-Bohus L 2003 *J. Vac. Sci. Technol.* A **21** 846–50
[28] Ehouarne L, Putero M, Mangelinck D, Nemouchi F, Bigault T, Ziegler E and Coppard R 2006 *Microelectron. Eng.* **83** 2253–7
[29] Nemouchi F, Mangelinck D, Bergman C, Clugnet G, Gas P and Labar J L 2006 *Appl. Phys. Lett.* **89** 131920
[30] Esconjauregui S, Whelan C M and Maex K 2007 *Nanotechnology* **18** 11
[31] Sutter E and Sutter P 2006 *Nanotechnology* **17** 3724–7
[32] Cui H, Yang X, Simpson M L, Lowndes D H and Varela M 2004 *Appl. Phys. Lett.* **84** 4077
[33] Merkulov I A, Merkulov V I, Melechko A V, Klein K L, Lowndes D H and Simpson M L 2007 *Phys. Rev.* B **76** 014109
[34] Wei Y Y, Eres G, Merkulov V I and Lowndes D H 2001 *Appl. Phys. Lett.* **78** 1394–6
[35] Chhowalla M, Teo K B K, Ducati C, Rupesinghe N L, Amaratunga G A J, Ferrari A C, Roy D, Robertson J and Milne W I 2001 *J. Appl. Phys.* **90** 5308–17
[36] Baylor L R *et al* 2004 *J. Vac. Sci. Technol.* B **22** 3021–4
[37] Melechko A V, Klein K L, Fowlkes J D, Hensley D K, Merkulov I A, McKnight T E, Rack P D, Horton J A and Simpson M L 2007 *J. Appl. Phys.* **102** at press